Electronic Supplementary Material (ESI) for Nanoscale.
This journal is © The Royal Society of Chemistry 2020

Electronic Supplementary Information for

Interfacial Nanomechanical Heterogeneity of *E. coli* Biofilm Matrix

Christian Titus Kreis,[a] Ruby May A. Sullan [a,b,*]

[a] Department of Physical and Environmental Sciences, University of Toronto Scarborough
[b] Department of Chemistry, University of Toronto
Correspondence: ruby.sullan@utoronto.ca

1 Experimental Details

1.1 Note on Biofilm Stability

The biofilms would generally disintegrate when using MilliQ water or PBS as the imaging medium—individual pieces detaching from the biofilm are readily observed, as early as five minutes. Frequently, edges of the biofilms (*E. coli* AR3110) started to detach from the membrane during the experiment.[1] However, parts of the biofilm which remain fixated on the petri dish can still be imaged. The complete biofilm could be detached from the membrane by gently shaking the petri dish with the sample. Although detached from the membrane, the biofilms did not disintegrate, but remained intact and still featured their characteristic macroscopic morphology, as seen in Video S3 of Ref 1). In contrast, biofilms in M9 medium or LB broth, can be imaged for several hours, without any signs of disintegration.

1.2 Quantitative Imaging

Force curve processing. The force curves were tilted by fitting a straight line individually to a fraction of the extend and retract raw data (usually between 0 and 50 % measured from maximal z-distance, i.e. the beginning of the extend cycle and the end of the retract cycle). Subsequently, this straight line was subtracted from the extend and retract data, respectively.

Topography. We tested two approaches to extract the topography of the QI-map from the individual force curves (Fig. S3). In the first approach, the algorithm detects the z-position (z-piezo) at which the force exceeds 80 % of the force setpoint, which generally identifies the z-position at which a stiffer material is indented. Consequently, this approach may capture the morphology of bacteria underneath a soft EPS layer (Fig. S3c, d). The second approach was to detect the z-position of the contact point, which more closely resembles the true topography of the sample, but with more noisy topography maps (Fig. S3e, f). We attribute this noise to uncertainties in contact point detection. Note that on a soft

material, the difference between both topography readings might be several hundreds of nanometers. All topography maps reported in this work are obtained using the first approach (force setpoint).

Apparent EPS layer thickness. To quantify the thickness of the EPS layer covering the bacteria in the biofilm, we introduced an apparent layer thickness parameter, defined as the distance between the contact point and the end point of the indentation curve (Fig. 1c and Fig. S4). The contact point is set as the point following the last zero-force intersection during the extend cycle. We tested using non-smoothed and smoothed data when detecting the contact point (Fig. S5). While using smoothed force curves appears to be superior at spots with soft EPS layer (Fig. S5a), it is also more prone to artifacts in other regions of the map (Fig. S5b,e). In case of non-smoothed force curves, we did not find any systematic artifacts, and the layer thickness maps appear to be more robust and reliable. Consequently, we use the apparent layer thickness maps obtained from non-smoothed data to visualize locations of EPS patches (Fig. S5d).The contribution of a stiff material (the bacteria) to the apparent layer thickness is small compared to any softer material (Fig. 3b: 80 nm of 400 nm as measured from zero separation, Fig. S17c: 30 of 600 nm). Note that the maximal possible indentation depth (before force threshold is exceeded) strongly depends on the material stiffness (1kPa: 2680 nm, 10 kPa: 847 nm, 100 kPa: 268 nm, 1 MPa: 84.7 nm at force threshold of 5 nN and with MLCT-BIO tip).

Pixel resolution and imaging time. The QI maps reported in this work are taken with pixel resolutions of 128 × 128 or 64 × 64 at physiological conditions. While this resolution may seem low when compared to contact and intermittent contact AFM imaging modes (1024 × 1024 pixels and higher), QI mode generates correlated maps of nanomechanical properties, in addition to topography. Comparable resolution is also possible in QI mode at the expense of imaging time. For instance, using our imaging parameters, a 64 × 64 QI map takes ~5 mins while a 1024 × 1024 would take ~ 20 hrs. Within longer imaging periods, physiology may change, and imaging becomes more susceptible to drift.

1.3 Two-Layer Linearized Hertz algorithm

We extract the elastic properties of the components of the biofilms (EPS and bacteria) with a linearized Hertz algorithm from the indentation curves. First, the algorithm identifies the data segment associated with EPS and bacteria by detecting a transition point between both regions. Therefore, we smooth the raw extend data with a moving average filter with window length 51, which seems optimal in our case (Fig. S20). Subsequently, the transition point is identified as the data point at which the smoothed data starts deviating significantly from the raw data (Fig. S21). The soft EPS layer is associated with the smoothed data prior to this transition point. The elasticity of the stiff bacteria is extracted from the raw data after the transition point, as the smoothed data does not coincide with the raw data in this segment. In both segments, the algorithm employs an individual set of parameters. Note that no analysis will be performed for the respective segment, if it is not present in the force curve (e.g. no significant soft EPS layer in the force curve).

In the next step, the algorithm identifies the part of each data segment that obeys Hertzian contact mechanics (Fig. 3b). In order to detect these data regimes, we use a linearized Hertz model, which was successfully applied to quantify the individual mechanical components of soft composite materials.[2–5] In Hertzian contact mechanics, the force response F on the cantilever when indenting a sample by depth d with a pyramidal tip is given by:

$$F = 0.7453\frac{E}{1-v^2}tan\alpha \bullet d^2, \qquad (1)$$

where α is the face angle of the pyramidal indenter, E the sample's elasticity, and v its Poisson's ratio.[6] In the linearized Hertz approach, the power law relationship between force and indentation given by the standard Hertz model (Eq. 1) is transformed to a linear relationship between the rescaled Force $\sqrt{F}$ and indentation depth, d:

$$\sqrt{F} = \left(0.7453\frac{E}{1-v^2}tan\alpha\right)^{\frac{1}{2}} \bullet d. \qquad (2)$$

That is, a linear regime of the transformed data represents a portion of the indentation curve that obeys Hertzian contact mechanics. In fact, any linear fraction of the transformed data can be ascribed to an individual layer in a complex, multilayered material, as previously demonstrated in a model bilayered PDMS system.[2]

To detect a linear region in the data associated with EPS segment (if present), the algorithm first attempts to fit a straight line to a fraction of the segment of the transformed smoothed data (Fig. 3b inset). The fitting process starts at the point following the last zero-force intersection in the smoothed transformed data (*black arrow* in Fig. 3b), which corresponds to the contact point for smoothed data (Fig. S4 and S5a). The default starting fit length in the EPS segment is 100 data points (twice the length of the smoothing filter). In case of a successful fit, fitting will be repeated with more data points until either the fit interval exceeds the end of the EPS segment at the transition point, or the fit is unsuccessful. The success of the linear fit is evaluated by its coefficients of determination (R^2 goodness of fit). The default threshold for a successful fit in this segment is $R^2 > 0.98$. If the initial fit is not successful, a new starting point will be selected (the point following immediately the previous starting point) and fitting starts over, as long as the end of the EPS segment has not been reached. In this context, we denote a successful fit as a successfully identified soft layer (Fig. S6).

Subsequently, the same iteration is repeated with the data segment associated with the stiffer underlying material, the bacteria. In contrast to the soft regime, the process is performed in reverse order starting at the last point in the indentation curve. The starting fit length in the bacteria region is 12 data points (2 % of data points in the indentation curve), the default threshold for a successful fit is $R^2 > 0.9$. A larger fit length is generally not possible in this segment, as the steep part of the indentation curve often contains fewer than 20 data points.

1.4 Three-Layer Linearized Hertz algorithm

The three-layer linearized Hertz algorithm has the same theoretical basis as the two-layer version, i.e. transformed indentation data is employed to find data regions that obey Hertzian contact mechanics (see Equation 1, 2 and the corresponding paragraphs). In the three-layer model, the algorithm first divides the indentation curve in up to three segments. Subsequently, the algorithm searches for a

linear regime in each segment, if present. Finally, the apparent Young's modulus is calculated for any successfully identified linear regime. As before, the success of the linear fit is evaluated by its coefficient of determination (R^2 goodness of fit).

In contrast to the two-layer algorithm, here the limits of each data segment are determined from an effective local elasticity. Therefore, the local slope of the transformed data is computed at each data point, which translates into an effective elasticity value. Based on results from the two-layer algorithm, the limits of the individual segments are local elasticities of 0 to 5 kPa, 5 to 250 kPa, and more than 250 kPa for the first, second, and third segment, respectively. In each segment, we employ an individual set of parameters to account for its specific characteristics. In the first segment, we use smoothed data and a starting fit length of 100 data points, while the threshold for a successful fit is $R^2 > 0.98$. In the second and third segments, we do not used smoothed data, as there may be a significant difference between smoothed and non-smoothed data in these segments (see discussion above). Moreover, these two segments generally contain fewer data points as the first segment. Taking both factors into account, the starting fit lengths are 75 and 10 data points for the second and third segments, respectively, while the R^2 thresholds are $R^2 > 0.95$ and $R^2 > 0.9$.

1.5 Cantilevers

We used four different commercially available probes that feature comparable cantilever spring constants, but different indenter geometries: MLCT-BIO-F (Bruker, USA), SNL-10-C (Bruker), qp-BioAC-CI-CB1 (NanoWorld AG, Switzerland), and NP-O10-A (Bruker) with a 6.46-µm diameter spherical silica bead (Bangs Laboratories, USA) attached to it. The MLCT-BIO-F cantilever featured a nominal spring constant of 0.60 N/m and resonance frequency of 125 kHz (calibrated values: k = 0.6 ± 0.1 N/m, f = 94.3 ± 2.13, N = 22) with a quadratic four-sided pyramidal tip (silicon nitride) with a face angle of 35±2 ° and a nominal tip radius of 20 nm. We note that due to the influence of hydrodynamics, it is impractical to use softer cantilevers, which slows down the imaging by a factor of 5 (Fig. S1). The SNL-10-C cantilevers (spring constant: nominal 0.24 N/m, calibrated: k = 0.35 ± 0.03, resonance frequency: 56 kHz, calibrated: f = 53.0 ± 1.04, N = 12) had an asymmetric, four-sided pyramidal silicon tip (front angle of 15±2.5 °, side angles of 22.5±2.5 °, and back angle of 25±2.5 °) with nominal radius of 2 nm. In contrast to the former two cantilevers, the qp-BioAC-CI-CB1 cantilever (spring constant: nominal 0.15 to 0.55 N/m, calibrated: k = 0.39 ± 0.04, resonance frequency: 65 to 115 kHz, calibrated: f = 85.1 ± 4,83, N = 8) had a conical, quartz-like tip with a cone half-angle of 15±3 °. Finally, the NP-O10-A cantilevers had a nominal spring constant of 0.35 N/m (calibrated: 0.546 N/m) and a resonance frequency of 65 kHz (calibrated: 62.3).

To calibrate the cantilevers, the sensitivity was measured by acquiring a force-distance curve on a glass slide. The sensitivity was obtained from a linear fit to the repulsive regime of the extend cycle. Subsequently, the spring constant and resonance frequency were determined from the thermal tune performed in air as implemented in the JPK software.[7] In all cases, a correction factor of 1 was used for calculating the spring constant.

1.6 Graphical Selection Tool

For a more targeted quantification of nanomechanical properties, we developed a graphical selection tool to identify individual features of the biofilm in the QI maps. In general, we use the topography map to identify individual bacteria (Fig. 5a) and the apparent layer thickness map to find patches of EPS coverage (Fig. 5b). Subsequently, the algorithm determines all force curves that were recorded at positions inside the polygon and assigns a user-defined identifier to them, for example "B1 to B6" and "EPS", for force curves corresponding to individual bacteria and EPS regions, respectively. This identifier can be used to access all corresponding force curves and quantities extracted from them. Thereby, the selection procedure provides a straightforward method for a robust analysis of the same biofilm features across multiple maps. It also facilitates to restrict the analysis to force curves that are generally less susceptible to artifacts: only force curves from the top of the bacteria are included in the analysis, while areas where the side of the AFM tip might have hit the bacterium are not part of the selections.

1.7 Geometry characteristics of AFM tip with spherical cap

Common indenter geometries used when probing elastic properties of biomaterials are spherical beads attached to tipless AFM cantilevers and AFM tips with either conical or pyramidal shape.[8–10] The uncertainties associated in determining the exact tip shape can explain the significant discrepancies in elasticity values obtained with varying indenter geometries—more especially in cases where the sample is indented only for a few tens of nm, e.g. when probing microbial and mammalian cells. Hundreds of nm indentation are often necessary to be able to assume a conical or pyramidal indenter geometry; as only then will the elasticity values become independent of the indenter geometry. The conical and pyramidal AFM tips generally feature a spherical cap with a radius of a few nanometers up to tens of nanometers at the end of the tip. For small indentation depths, the indenter geometry of these AFM tips cannot be accurately described, as the tip transitions from spherical cap to conical/pyramidal shape. The conical or pyramidal shape only comes into effect after tens of nanometer (nm) indentation, for example after approximately 18.9 nm indentation for a cone with a 35 ° half angle and tip radius of 20 nm (Fig. S22). This uncertainty in the exact determination of tip geometry can explain the significant discrepancies in elasticity values obtained with varying indenter geometries—more especially in cases where the sample is indented only for a few tens of nm, e.g. when probing cells. Thus, hundreds of nm indentation are necessary to be able to assume a conical or pyramidal indenter geometry; as only then will the elasticity values become independent of the indenter geometry.

1.8 Elasticity Measurement on model PDMS substrate

Sample preparation. Polydimethylsiloxane (PDMS) samples were prepared from SYLGARD™ 527 Silicon Dielectric Gel (Dow Silicones Corporation, US) following the standard procedure (mix both parts Gel Part A and Gel Part B in 1:1 ratio). The mixture was degassed by centrifuging at 1400 g for 3 min. Subsequently, the gels were poured into small petri-dishes and cured at 75 °C for 6 hours. PDMS substrates were imaged in ethanol to reduce adhesion between the tip and the sample.

Elasticity measurements on PDMS substrates. Using four different indenter geometries: spherical cap (NP-O), pyramidal (MLCT-BIO and SNL), and conical (qp-BioAC-CI), on a model PDMS substrate, we found a good agreement between elasticity values with hundreds of nm indentation (Fig. S10). As

such, in our biofilm samples, we determine the elasticity of the EPS matrix from indentation curves with at least a few hundreds of nm indentation.

1.9 Data Visualization and Statistics

Boxplots. We report the calculated apparent Young's modulus in boxplots, where the upper and lower limit of the box represents the 75^{th} and 25^{th} percentile, respectively, while the solid line represents the median. The whiskers extend from the box to the furthest data point within 1.5× the interquartile range (size of the box). Outliers, i.e. data points beyond 1.5× the interquartile range are omitted.

Force curves statistics. The number of force curves in each QI map per biofilm sample are indicated inside figures or in figure captions. The statistics pertaining to Fig. 6c and Fig. 7b are reported in ESI † Tables 1 and 2, respectively.

2 Electronic Supplementary Information (ESI) Figures

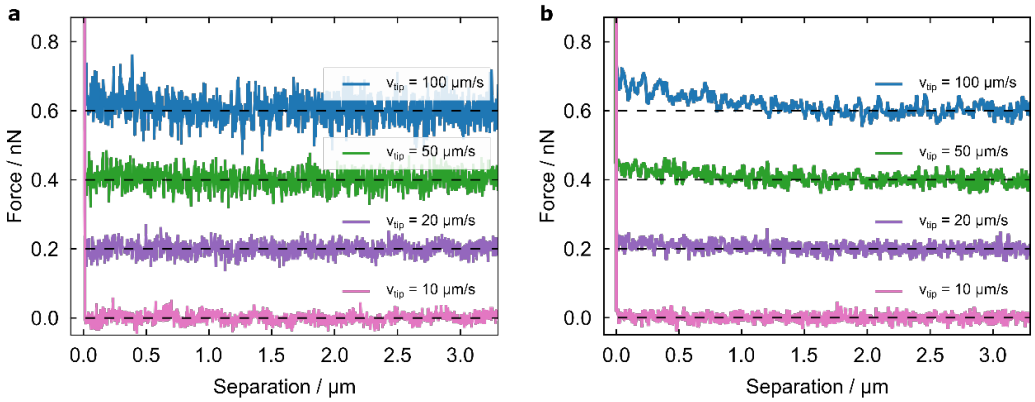

Fig. S1 Effect of hydrodynamics in QI mode for different tip velocities. A glass substrate was imaged in water with different tip velocities. **(a)** Sample indentation curves obtained for different tip velocities with the default MLCT-BIO-F cantilever (nominal spring constant k = 0.6 N/m, calibrated: k = 0.648 N/m). Some indentation curves indicated that there might be a repulsive deflection tens of nanometer prior to contact at a tip velocity of 100 µm/s. We highlight that we did not observe that signature consistently, as it is the case for the softer cantilever. No such deflection was observed for tip velocities of 50 µm/s and below. **(b)** Sample indentation curves obtained with a soft MLCT-BIO-D cantilever (nominal spring constant k = 0.03 N/m, calibrated: k = 0.043 N/m). A repulsive deflection of the cantilever can be observed at high tip velocities as early as 1.5 µm prior to contact. The magnitude of this effect decreases with decreasing tip velocity and vanishes at a tip velocity of 10 µm/s. Most of the reported data in this study are from 5 × 5 µm² QI maps, with a grid of 64 × 64 force curves (total of 4096), with each cycle (extend and retract) of the force curve having 600 data points.

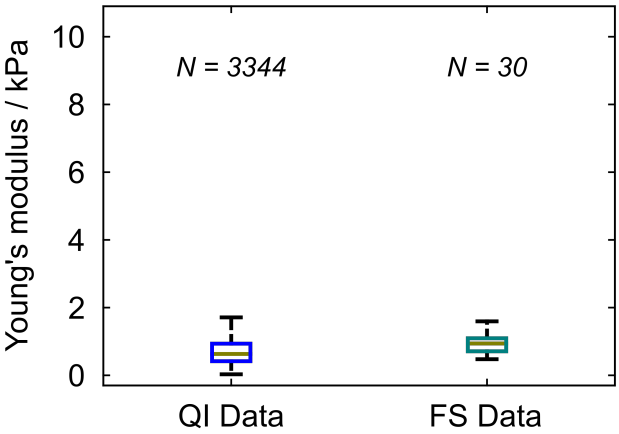

Fig. S2 EPS elasticities of *E. coli* AR3110 biofilm obtained from QI mode and force spectroscopy mode (FS) with two-layer linearized Hertz algorithm. The force curves in FS and QI mode were recorded at the exact same location featuring Type 3 morphology. QI mode was imaged with 50 µm/s tip velocity, while FS mode was imaged with 2 µm/s. The other force curve parameters (set point, z-range) were kept constant.

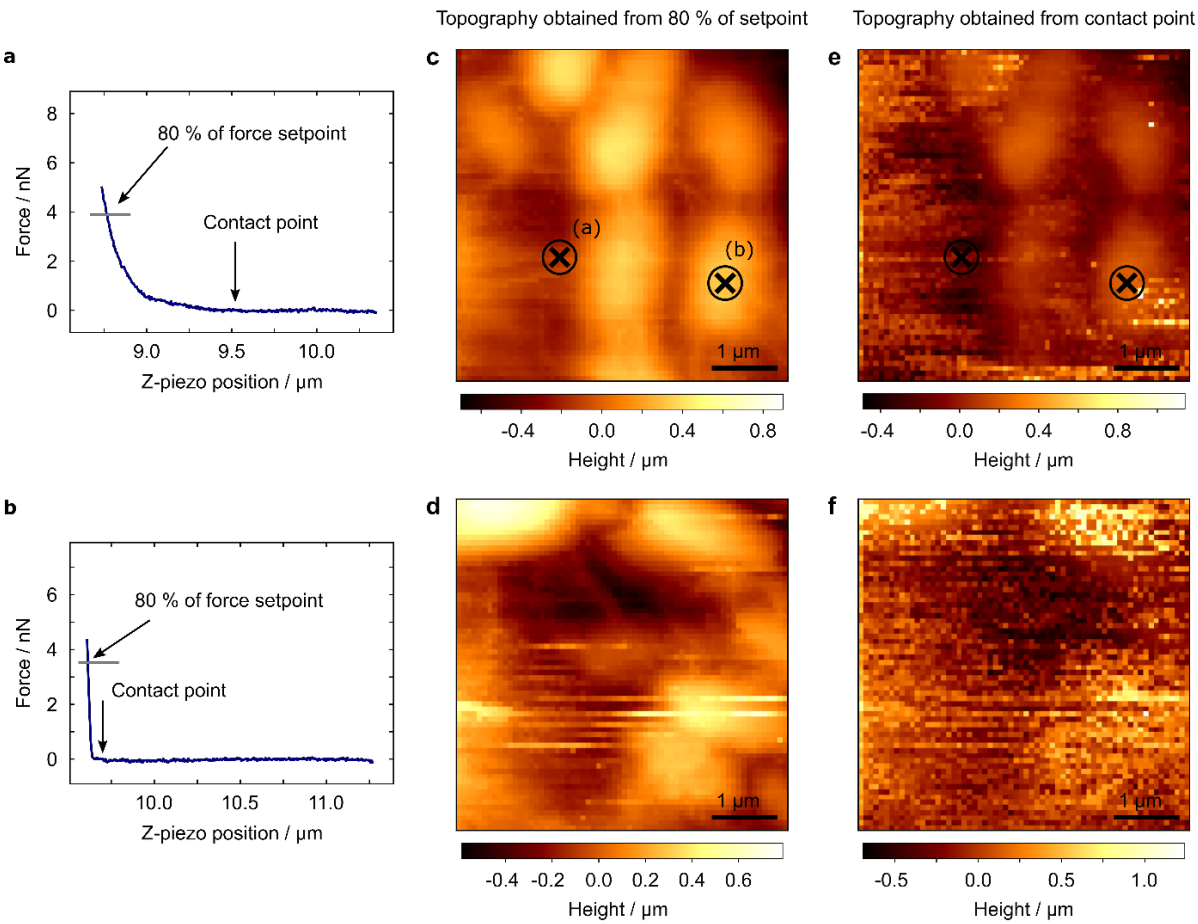

Fig. S3 Comparison of different approaches to extract the topography of a QI map. **(a)** Force-distance curve at a location with thick EPS layer. In this case, the difference between both topography readings may be up to several hundreds of nanometer. **(b)** Force curve recorded on top of a bacterium. There is only a minor difference in the position of the topography points. **(c)-(d)** Topography map as obtained by extracting topography at 80% of the force setpoint. Locations of force curves shown in (a) and (b) are marked. **(e)**–**(f)** Topography map obtained from the contact points for the same QI maps as shown in (c) and (d), respectively. Note that some of the bacteria visible in the (c), (d) become invisible, especially when the whole map is covered with a EPS layer (f).

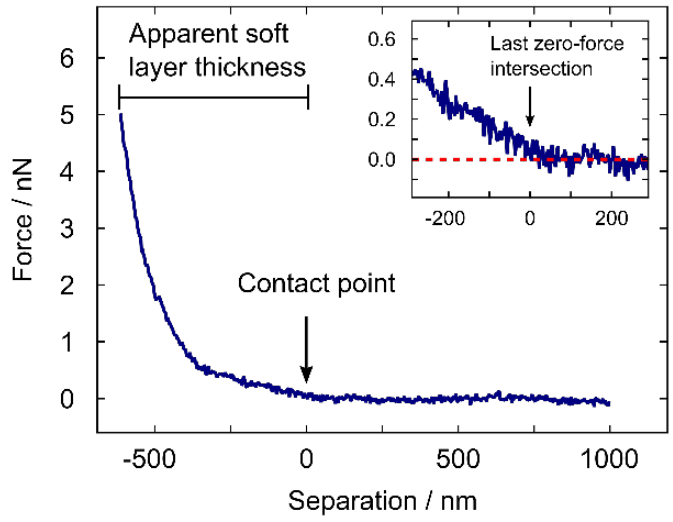

Fig. S4 Apparent layer thickness. We define the apparent layer thickness as the distance between the contact point and the end of the force-distance curve (in the extend cycle). The contact point is set as the point of the last zero-force intersection.

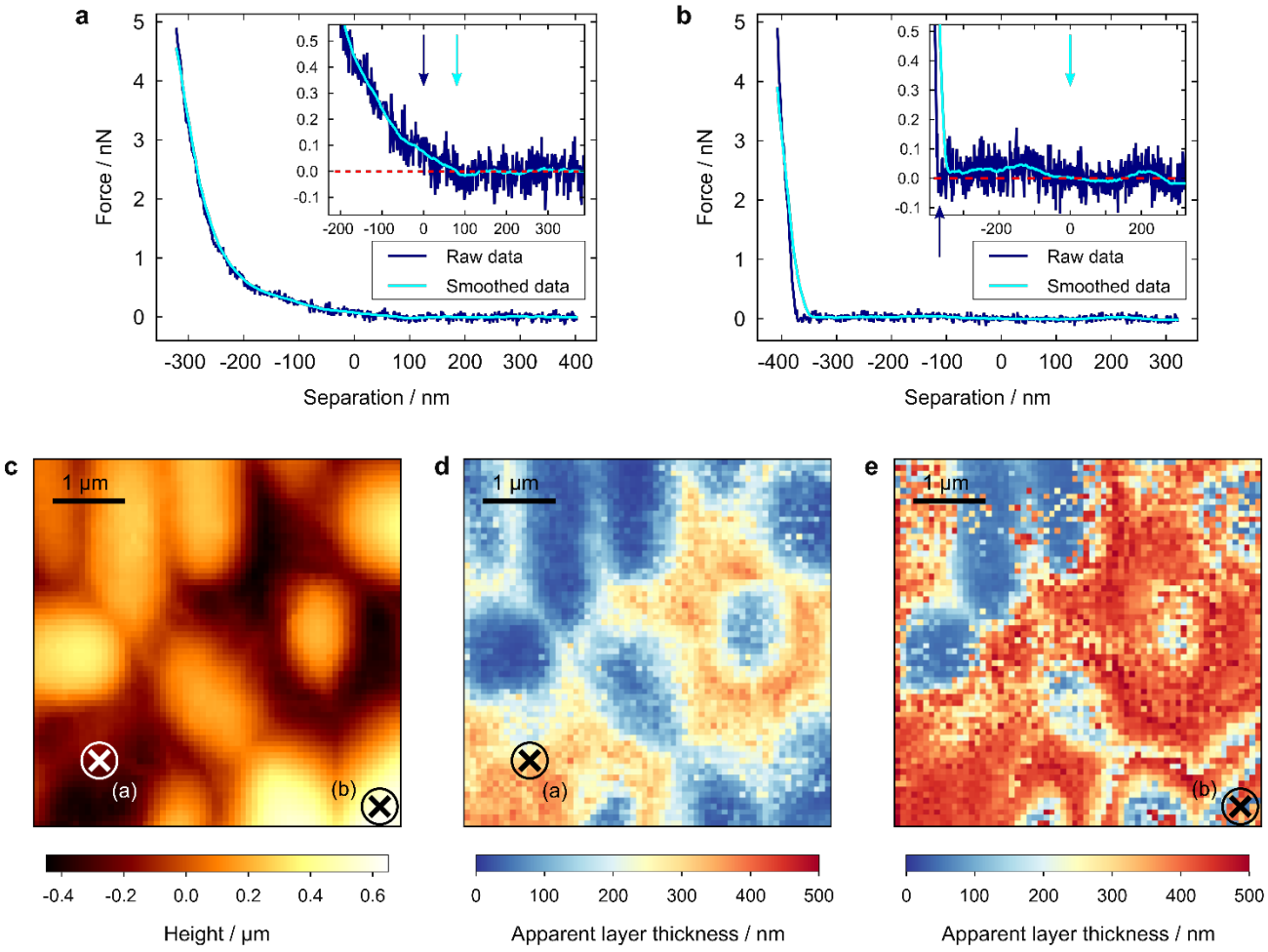

Fig. S5 Influence of contact point implementation on soft layer thickness. **(a)** Extend cycle of force curve on a spot with significant EPS layer, marked in (c) and (d). Inset: Difference of contact point location based on using non-smoothed data (default algorithm, *blue*) and smoothed data (*teal*), respectively. In both cases, the contact point is implemented as the point of the last zero-force intersection (see also Figure S4). The contact point obtained from the smoothed data seems to resemble the true contact point more closely. Note: The *z*-range of the force curves in this QI-map was 1000 nm. **(b)** Extend cycle of force distance curve on a bacterium, marked in (c) and (d). The contact point from the smoothed data (*teal*) is shifted by several hundreds of nanometer compared to the point from the non-smoothed data (*blue*) due to a weak undulation in the baseline. The contact point from the non-smoothed data seems to be closer to the true contact point. **(c)** Topography of *E. coli* biofilm. **(d)** Apparent layer thickness as obtained with the default contact point implementation (no data smoothing). **(e)** Apparent layer thickness for contact points extracted from smoothed data. The EPS layer appears to be larger in regions without bacteria, while regions with bacteria feature data analysis artifacts as demonstrated in (b). Additionally, there seem to be a rather sharp transition at the edges of EPS patches, where the layer thickness drops instantaneously from above 400 nm to below 100. This consistent sharp drop seems rather unlikely for EPS patches in a biofilm sample.

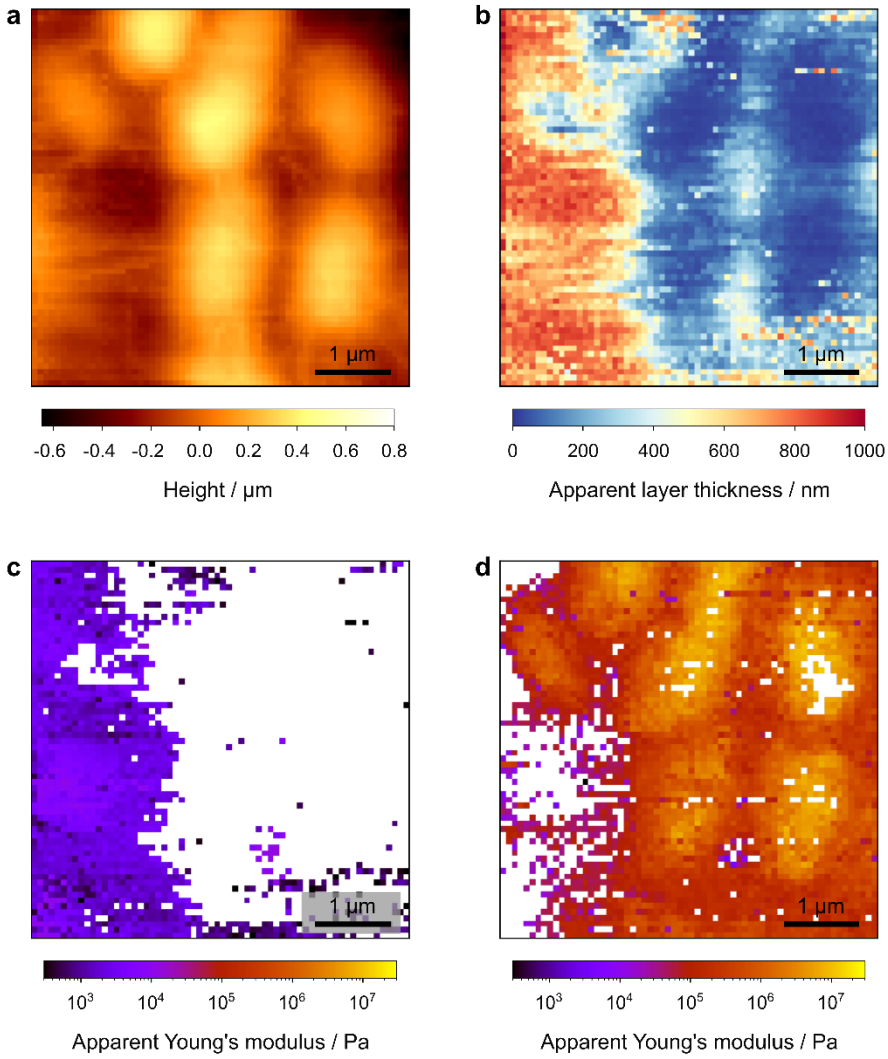

Fig. S6 Elasticity maps obtained from two-layer linearized Hertz algorithm. **(a)** Topography of *E.coli* biofilm. **(b)** Apparent layer thickness map reveals a patch of thick EPS on the left side. **(c)** Elasticity of layer 1 in the linearized Hertz algorithm. White pixels correspond to indentation curves, where the algorithm did not successfully identify a soft layer. This outcome can either be due to too little data points in the soft layer segment to perform a fit, or the goodness of fit (R^2 value) of the linear fit to the transformed data was lower than the defined threshold. We note that adjusting the relevant parameters (starting fit length, goodness of fit threshold) in the algorithm influences the fraction of force curves with an identified linear regime. Reducing the R^2 threshold and/or lowering the starting fit length results in a larger fraction of force curves with successfully identified linear regimes, but it also compromises the overall quality of the fits. **(d)** Elasticity of layer 2 in the linearized Hertz algorithm.

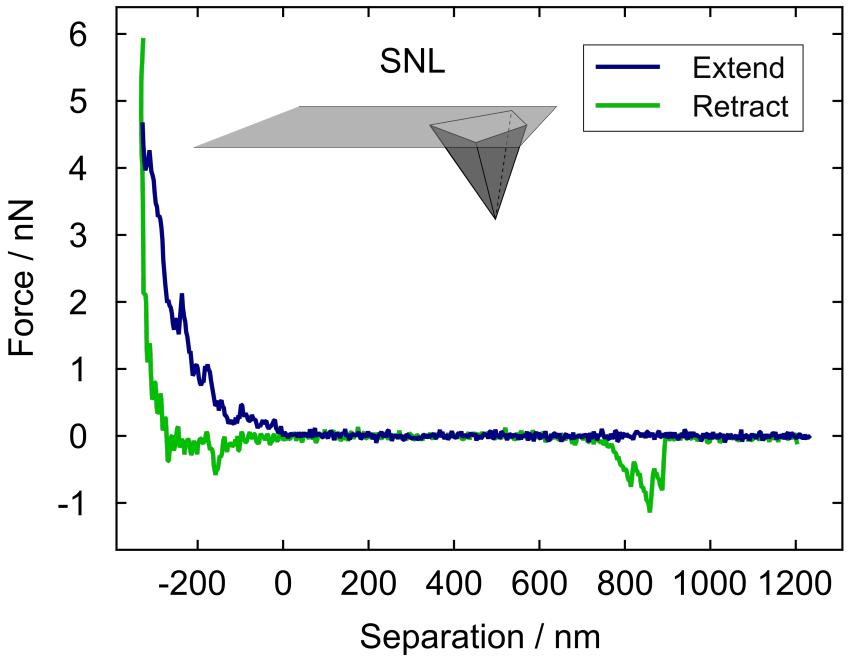

Fig. S7 Sample force curve from QI map recorded with SNL tip on *E. coli* AR3110 biofilm (default scanning parameters). The adhesion signatures at hundreds of nanometer tip-sample separation are most likely long polymer chains being pulled out of the EPS matrix.

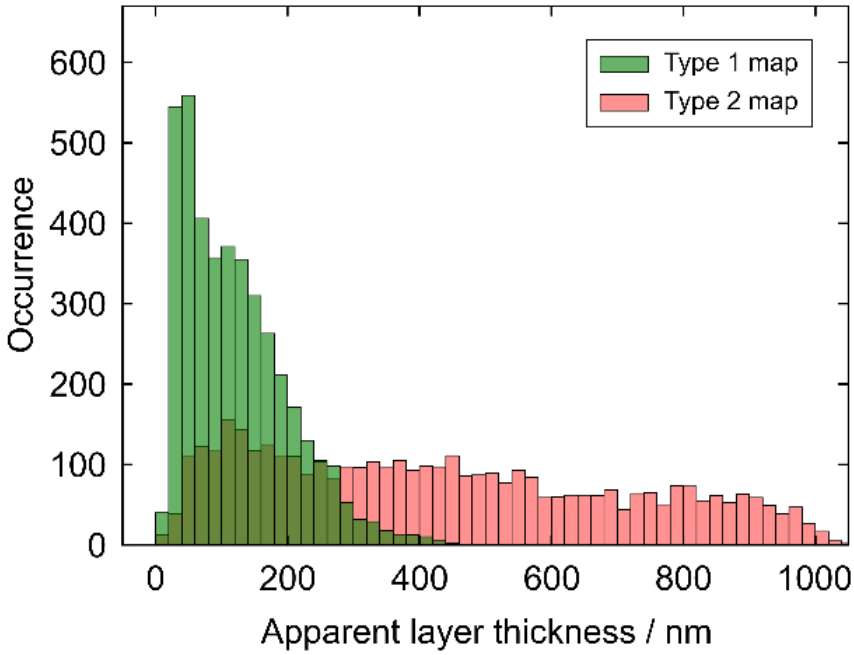

Fig. S8 Apparent layer thickness for QI maps of different type. Distributions of apparent layer thickness from the QI maps shown in Fig. 2a,b highlight the difference between Type 1 (*green, N = 4096*) and Type 2 maps (*red, N = 4096*).

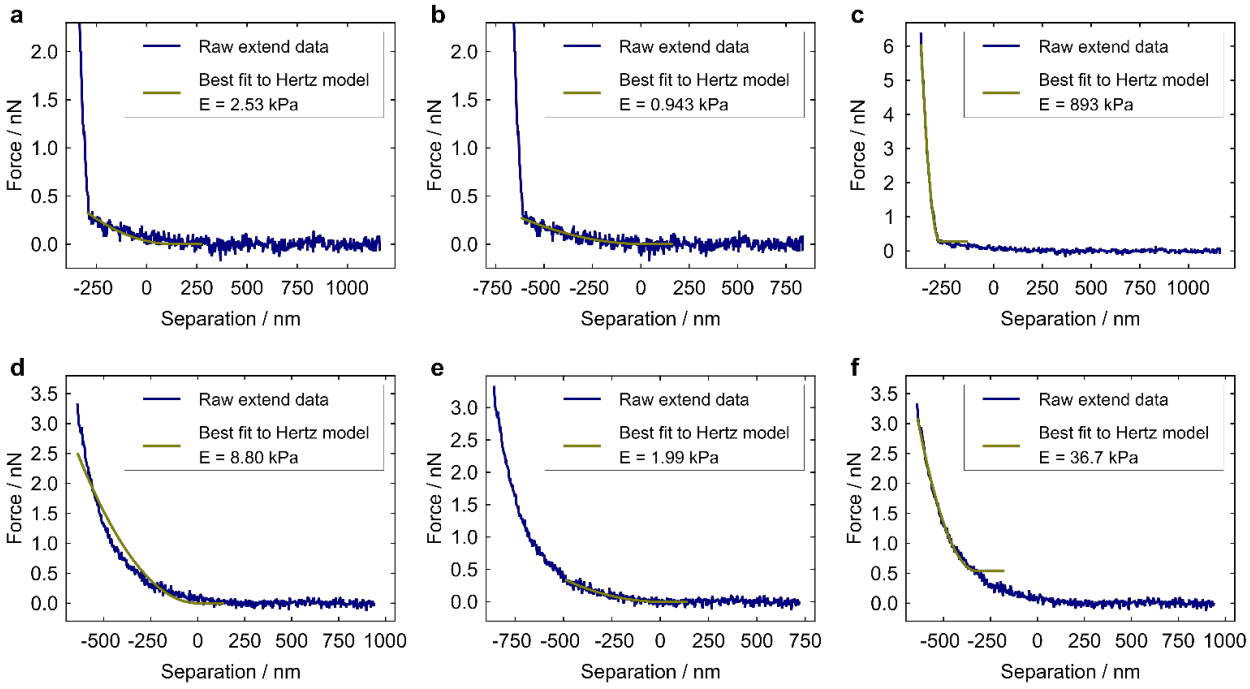

Fig. S9 Limitations of standard Hertz Model. The best fit to the Hertz model is shown for different implementations. **(a)** Optimal fit range manually set, contact point determined from non-smoothed data. **(b)** Optimal fit range manually set, contact point determined from smoothed data. The fit captures the first part of the indentation curve, while the second part is omitted. **(c)** Dynamic contact point: Each data point in the curve is set as a start point (i.e. contact point) for a fit. The fit with the smallest residuals is selected as the final fit. This implementation captures the second part, while misses the first part. **(d)** A fit to the whole data range cannot describe the multi-layer indentation curve. **(e)** Optimized fit range manually set, contact point from smoothed data. This implementation may describe the first part of the force curve. Note that the fit range is different compared to the force curve shown in (b). **(f)** Dynamic contact point.

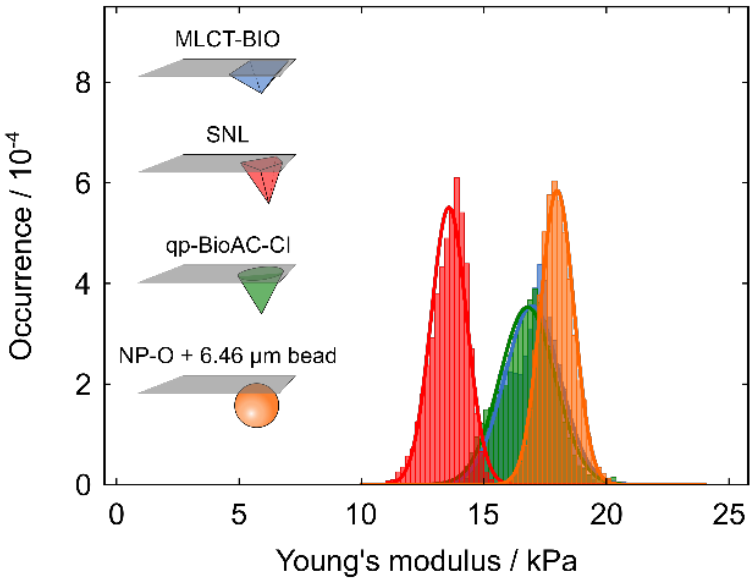

Fig. S10 Comparison of indenter geometry on model sample. Distribution of Young's moduli of the same PDMS Sylgard© 527 sample measured with four

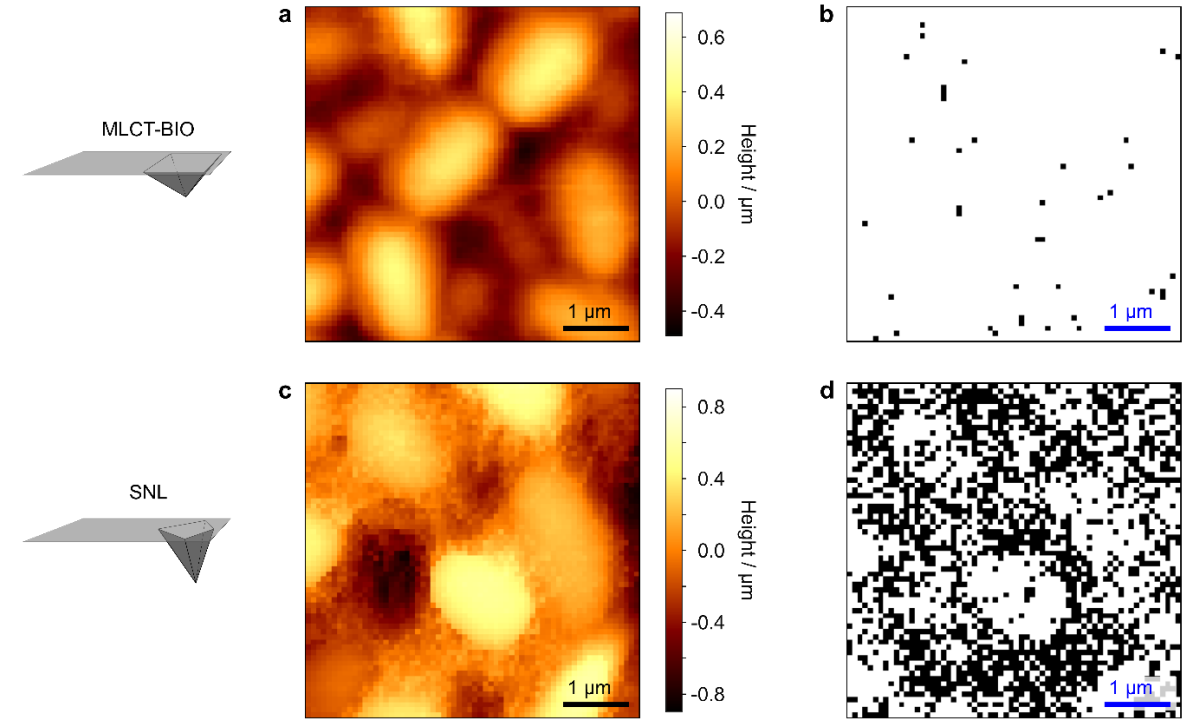

Fig. S11 Location of force curves with breakthrough events (black pixels) on same biofilm sample. **(a)** Biofilm topography obtained with MLCT-BIO tip. **(b)** Location of force curves with breakthrough events (*black spots*). **(c)** Biofilm topography obtained with SNL tip. **(d)** Location of indentation curves with breakthrough events (*black spots*). The chance for breakthrough events appears to be smaller in force curves recorded on bacteria (without EPS cover).

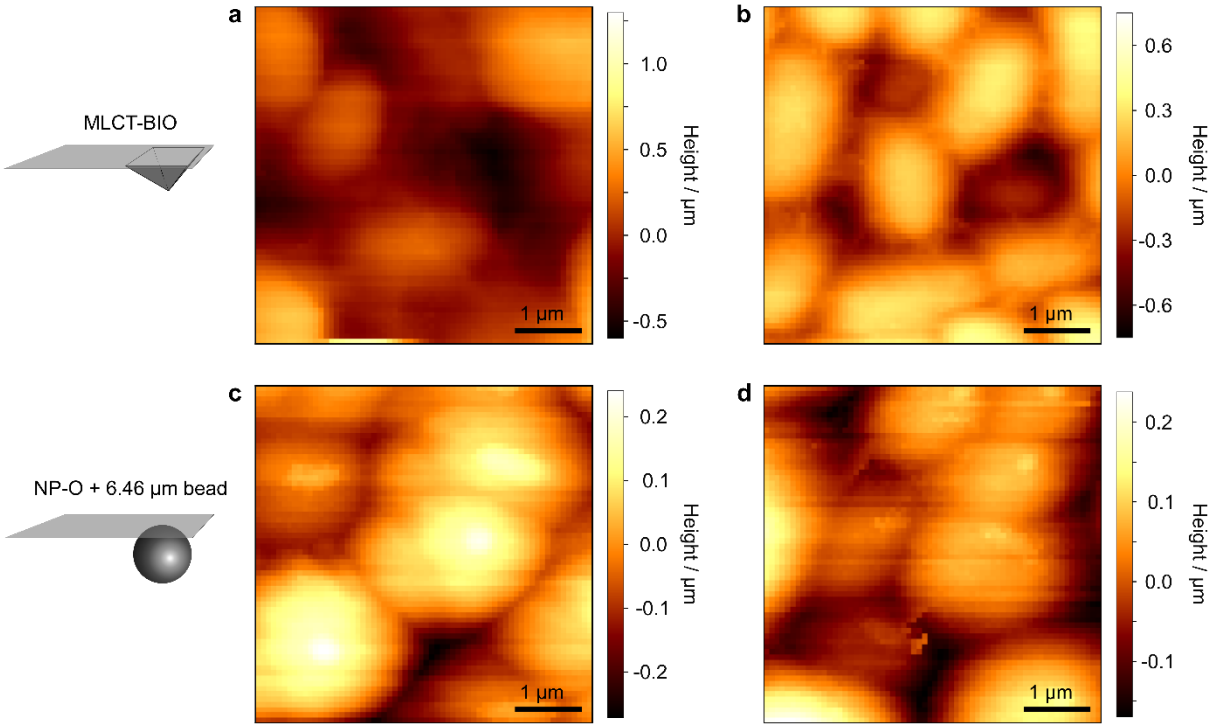

Fig. S12 Influence of indenter geometry on structural resolution in biofilm imaging. **(a,b)** Biofilm topography obtained with MLCT-BIO tip. The shape of the *E. coli* bacteria is retained. **(c,d)** Biofilm topography obtained with a spherical bead as tip. The shape of any features in the topography map is distorted by the tip geometry.

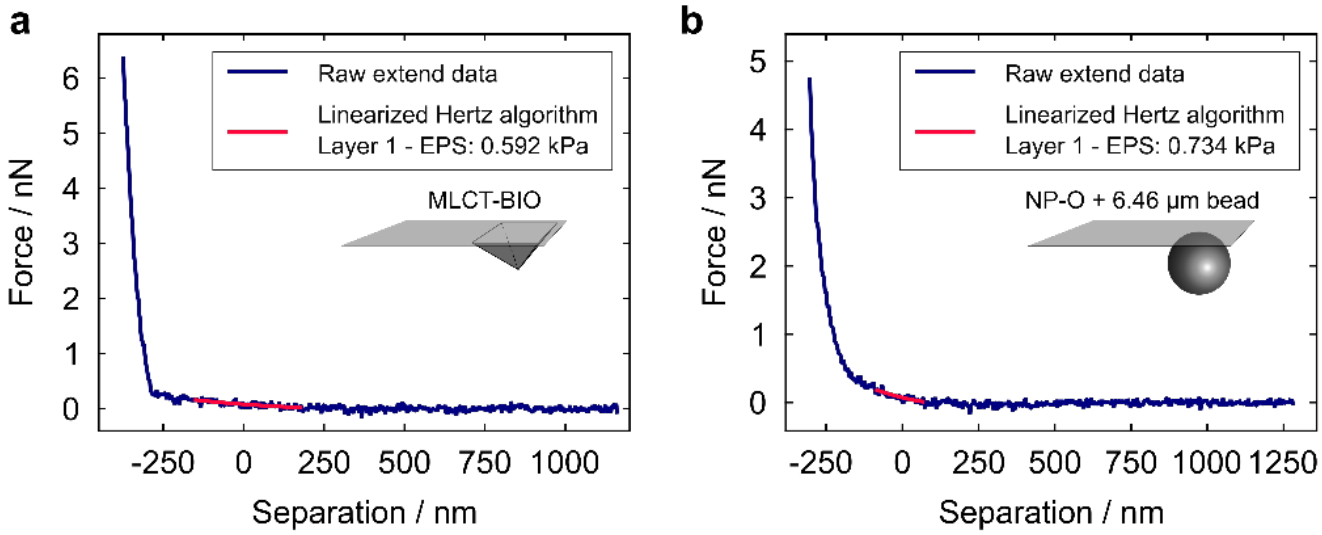

Fig. S13 Comparison of EPS elasticities for different indenter geometries. The two-layer linearized Hertz algorithm was used to determine EPS elasticity; the second layer (bacteria) is not shown. **(a)** Force curve recorded with MLCT-BIO tip. **(b)** Force curve recorded with NPO tip with bead. The fit range was reduced to 50 data points (from a default of 100 data points), as a fit was not possible otherwise.

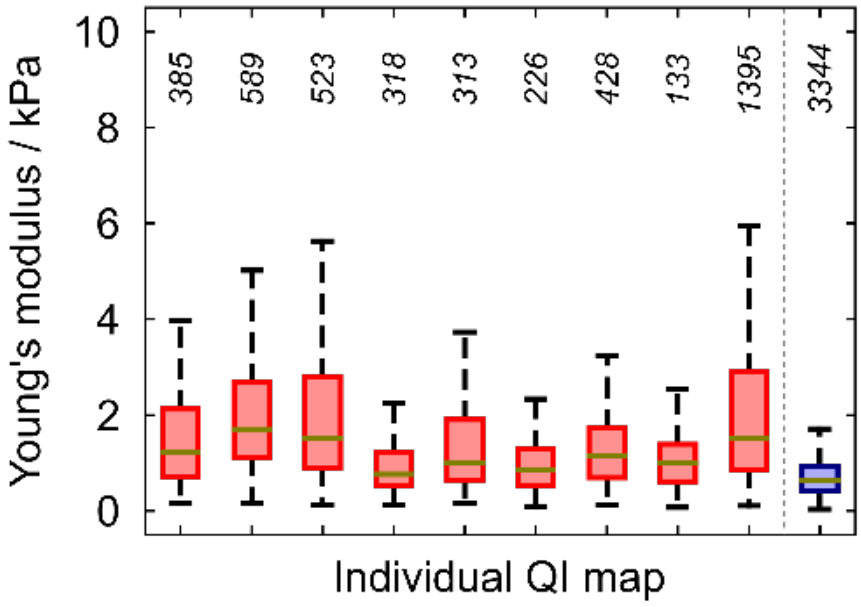

Fig. S14 EPS elasticities of individual QI maps from the same biofilm. The Type 2 distributions (*red*, left) exhibit some variations between individual QI maps and feature larger elasticity values than the Type 3 distribution (*blue*, right).

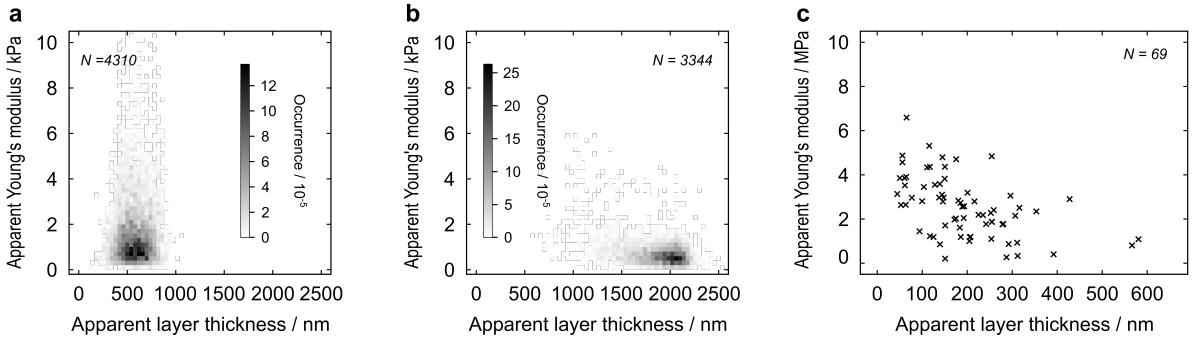

Fig. S15 Elasticity versus apparent layer thickness. **(a)** Relative occurrence of EPS elasticity as function of apparent layer thickness for QI maps with Type 2 morphologies (mix of bacteria and EPS). There does not seem to be a correlation between EPS elasticity and layer thickness. Data of force curves from EPS selections of biofilm #3 (see Table 1) are shown. **(b)** Relative occurrence of EPS elasticity as function of apparent layer thickness for a QI map with Type 3 morphologies (predominantly EPS, biofilm #3). **(c)** Mean elasticity of bacteria versus mean apparent layer thickness covering each individual bacterium.

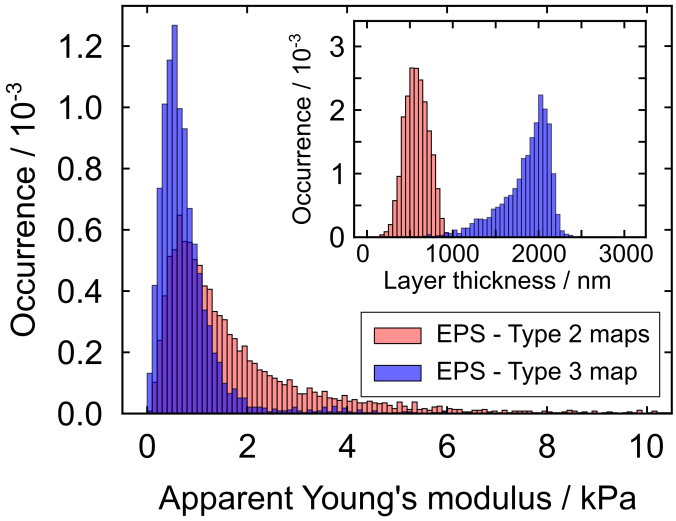

Fig. S16 Comparison of EPS elasticities from different local biofilm morphologies. The cumulative distribution of EPS elasticities for Type 2 (*red,* 9 maps, *N = 4310*) and Type 3 (*blue*, 1 map, *N = 3344*) of the same biofilm(biofilm #3, see Table 1) are shown. *Inset*: Distribution of soft layer thickness of EPS patches included in the analysis. The Type 2 distribution features a tail at larger elasticity values compared to the Type 3 map distribution. As the apparent layer thickness is approximately 2 to 3 times smaller at the EPS spots in the Type 2 maps than in Type 3 maps, this difference in EPS elasticity values could be due to a contribution of their underlying material (i.e., thick EPS for Type 3 vs. bacteria for Type 2). However, we could not thoroughly test this hypothesis due to lack of data for layer thicknesses in the 1000 to 1500 nm range. Nevertheless, the spread of the elasticity distribution is significantly larger at lower layer thicknesses. See also Figure S15a,b for a correlation between elasticity and layer thickness individually for Type 2 and Type 3 maps, respectively.

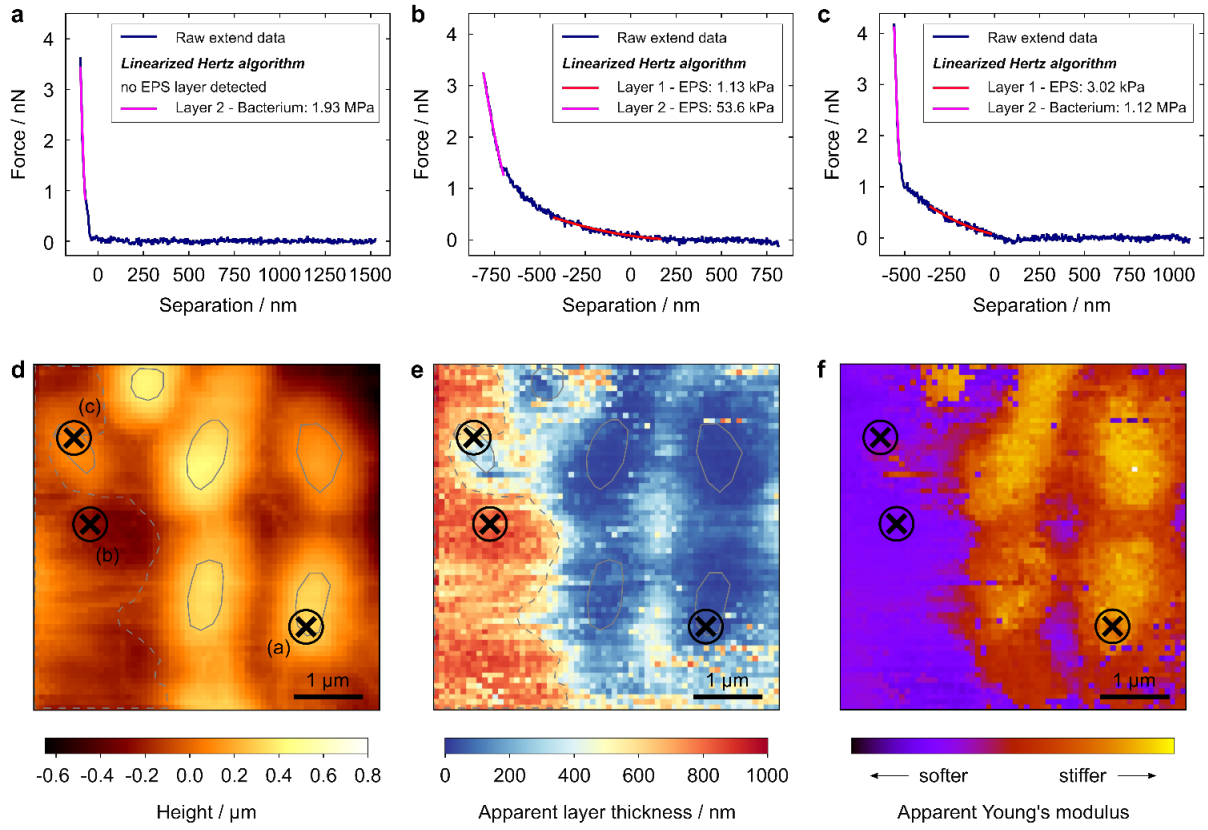

Fig. S17 Sample force curves from different biofilm features. **(a)** Force curve recorded on a bacterium (*pink* line, E = 1.93 MPa) exposed at the biofilm surface (without any EPS cover). **(b)** Force curve recorded at a location with a thick soft layer (*red* line, E = 1.13 kPa). The force curve features an underlying material with an apparent Young's modulus of tens of kPa (*pink* line, E = 53.6 kPa). **(c)** Force curve recorded on a bacterium (*pink* line, E = 1.12 MPa) covered with a soft EPS layer (*red* line, E = 3.02 kPa). **(d)** Topography of biofilm. The location of the indentation curves shown in (a) to (c) are marked with black crosses. The individual bacteria, as well as the EPS spot are outlined in grey (compare the graphical selection tool introduced in Fig. 5). **(e)** Apparent soft layer thickness map of biofilm. **(f)** Estimated elasticity of biofilm.

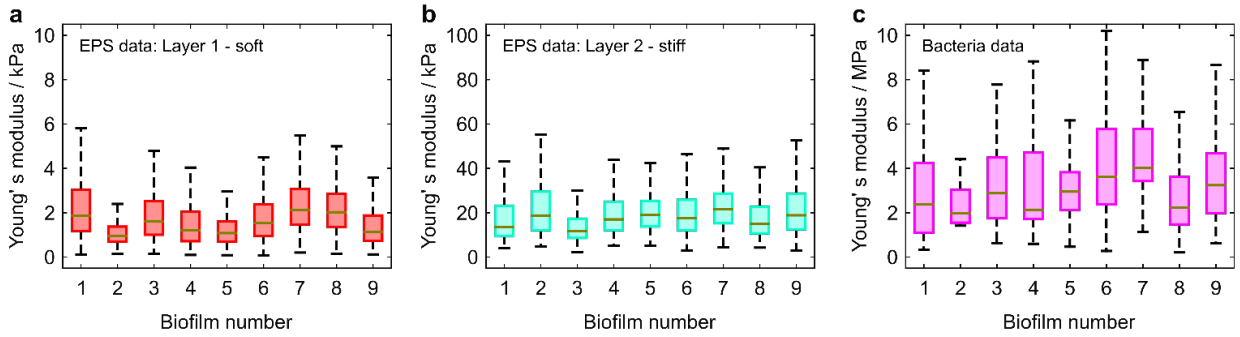

Fig. S18 Heterogeneity in EPS in *E. coli* biofilms. Elasticities were obtained with three-layer linearized Hertz algorithm. For a comparison in one graph see Fig. 7. **(a)** Layer 1: Soft EPS. **(b)** Layer 2: Stiff EPS.

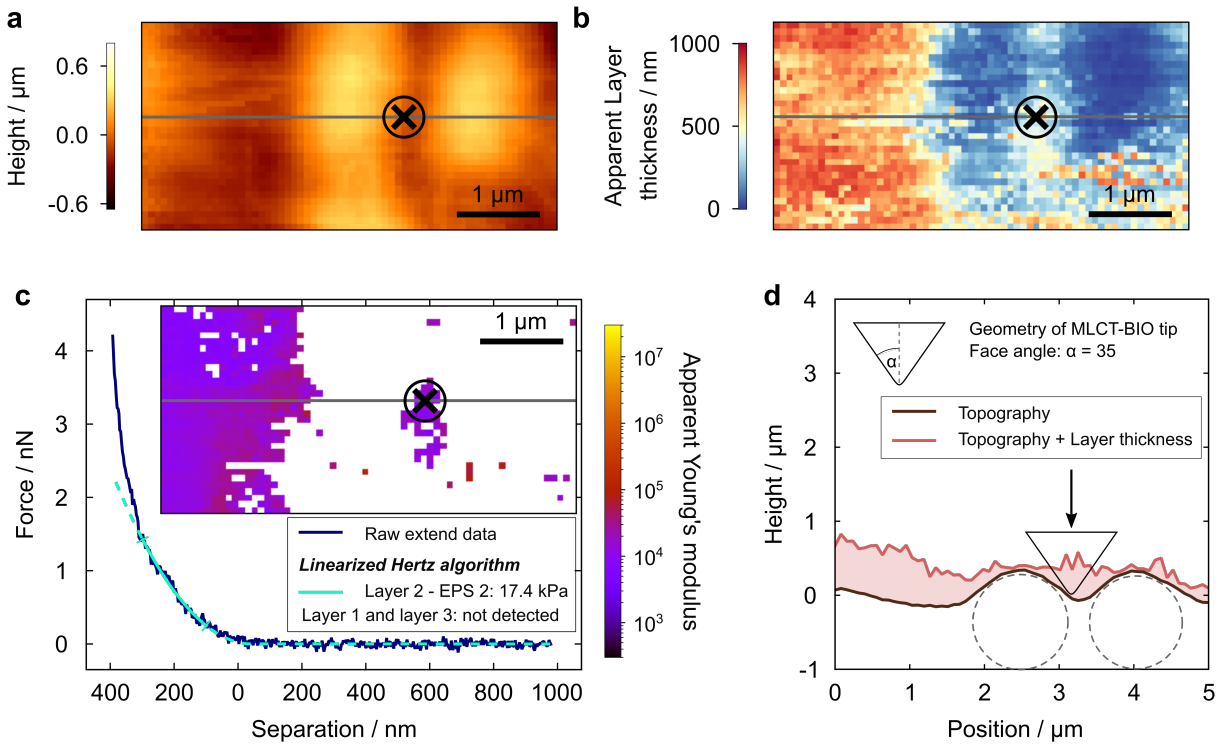

Fig S19 Characteristics of EPS between bacteria. **(a)** Topography of biofilm. Section of QI map shown in Fig. 5, Fig. S15. **(b)** Apparent layer thickness of biofilm section. **(c)** Force curve recorded in between two bacteria. The position is shown in a,b (cross), and d (arrow). The three-layer linearized Hertz algorithm detected an EPS layer with 17.4 kPa elasticity. Inset: Location of stiff EPS (layer 2) in the biofilm shown in a,b. The analysis reveals stiff EPS in between the two bacteria. **(d)** Biofilm morphology of individual scan line (*grey* line in a,b, inset in c). The location of two bacteria is indicated with a dashed line. The geometry of the MLCT-BIO tip is shown as comparison at the end of the indentation process. The sketch demonstrates that the side of the tip did not touch the bacterium for several hundreds of nanometer indentation at the location of the force curve (arrow).

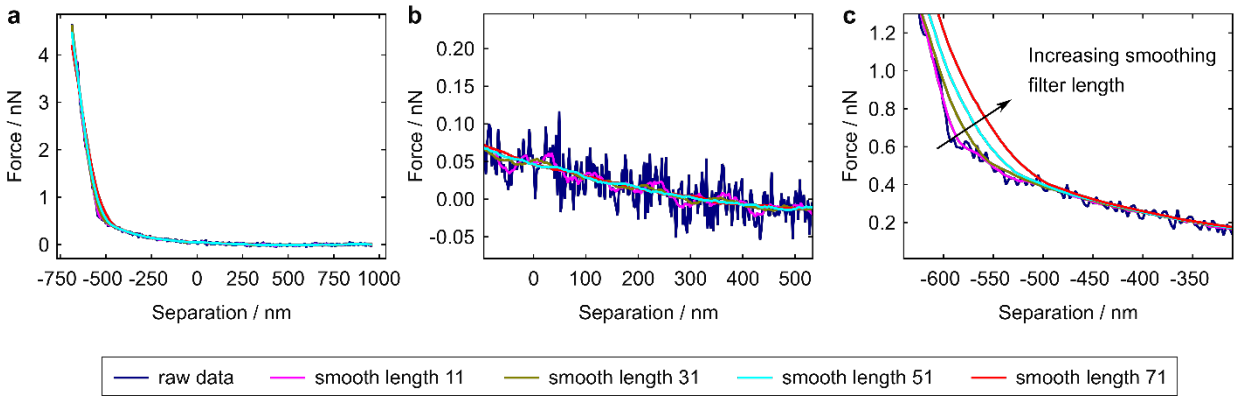

Fig. S20 Influence of smoothing filter window length. **(a)** Raw extend data (*blue*) and data smoothed with a first-order Savitzky-Golay filter of different length: 11 (*pink*), 31 (*olive*), 51 (*teal*), and 71 (*red*). Note that a first order Savitzky-Golay filter is identical with a moving average filter, but allows for more flexibility with the same algorithm syntax, such as using a higher filter order for data smoothing. **(b)** Data section around the contact point. A filter window length of 11 exposes a weak erratic undulation in the data. This undulation is suppressed by using a filter with window length 51. **(c)** Data section around the transition region from soft to stiff material, here around negative 500 to 600 nm separation. An increased filter window length results in an earlier deviation from the raw data in the transition region. A filter window length of 51 data points seemed the best compromise between suppressing any weak erratic undulation and a later deviation from the raw data.

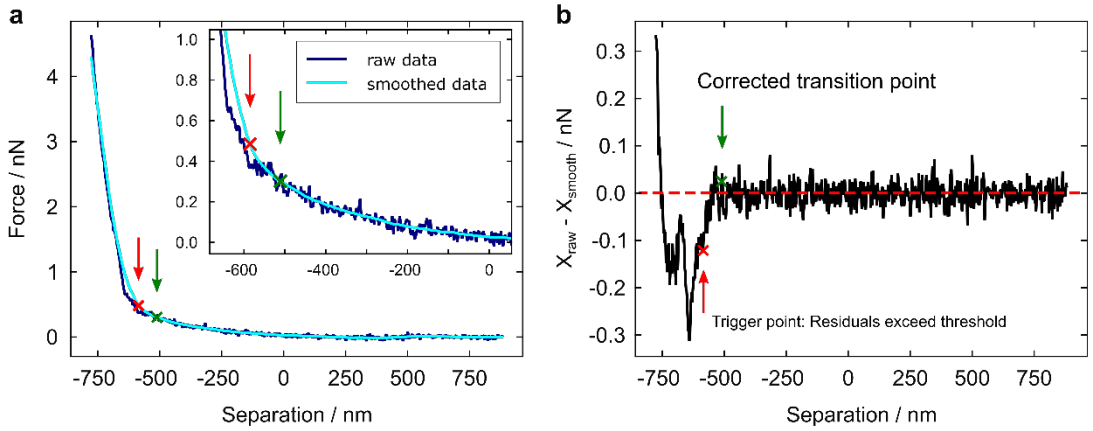

Fig. S21 Detection of transition point. **(a)** Raw extend data (*blue*) and data smoothed with default Savitzky-Golay filter (*teal*, length 51, order 1). The transition point and a trigger point are shown with green and red marker, respectively. Inset: Data section in the transition region. **(b)** Difference between raw data (X_{raw}) and smoothed data (X_{smooth}) shown in (a). The algorithm detects a trigger point at which the difference between both data sets exceeds a given threshold (*red* marker, arrow). The default threshold is 5 times the standard deviation of the difference data (first 20 %, corresponds to the first part of the baseline). Correcting the trigger point with half the filter window length results in the transition point (*green* marker, arrow).

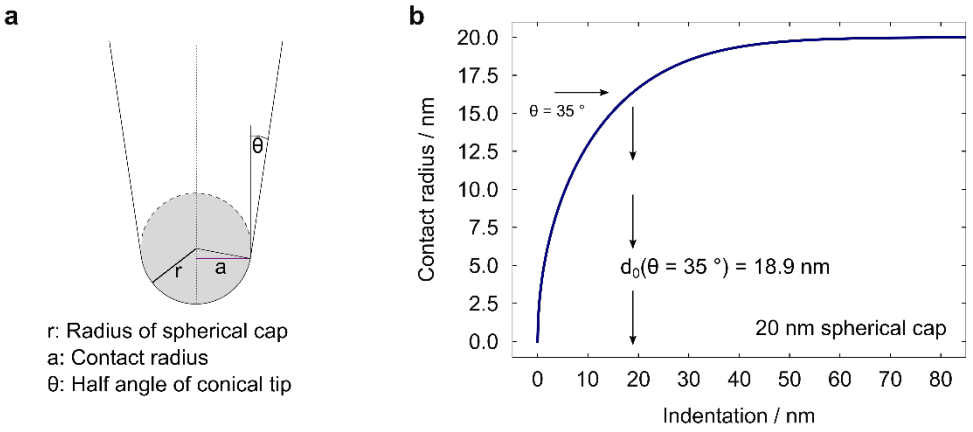

Fig. S22 Geometry characteristics of AFM tip with spherical cap. **(a)** Sketch of cantilever with spherical cap. **(b)** A conical AFM tip with spherical cap transitions at the critical indentation depth d_0 from a sphere into the cone. At this point the contact radius a_0 is given as $a_0 = r*\sin(90 - \Theta)$. The contact radius a of a sphere and indentation depth d are related via $d = a/2*\ln(r+a/r-a)$. Thus, for a cone with 35 ° half angle with spherical cap of radius 20 nm, the critical indentation depth is $d_0 = 18.9$ nm.

3 Electronic Supplementary Information (ESI) Tables

Table 1. Statistics of biofilms in Figure 6

Biofilm #	QI maps	Bacteria selections		EPS selections	
	Count	Count	FD* curves	Count	FD curves
1†	10	55	3702	4	2101
2	6	24	1938	1	84
3†	12	69	4958	17	4310
4†	6	31	1850	5	3280

*FD: number of successfully analyzed Force-Distance curves
†Maps also analyzed with three-layer algorithm for Figure 7
Note that for biofilm #3, the Type 3 map was omitted from the EPS analysis in Figure 6. The Type 3 map is also not included in the statistics..

Table 2. Statistics of biofilms in Figure 7

Biofilm	QI maps	Bacteria selections		EPS selections			
	Count	Count	FD* curves	Count	FD* Curves - Soft	FD* Curves - Stiff	FD Curves - Both
1†	10	56	3168	7	2446	1220	435
3†	12	63	3303	18	3943	1220	380
4†	6	24	1195	6	3123	2237	778
5	7	22	1600	6	5647	4952	2989
6	3	10	517	5	4213	509	297
7	8	36	1703	10	12056	4619	3554
8	10	43	3401	11	8268	2055	1215
9	10	75	3011	4	1634	1719	855
10	10	57	2832	9	3347	1486	385

*FD: number of successfully analyzed Force-Distance curves
†Maps also analyzed with two-layer algorithm for Figure 6

4 References

1 D. O. Serra, A. M. Richter and R. Hengge, *J. Bacteriol.*, 2013, **195**, 5540–5554.
2 G. Kaushik, A. Fuhrmann, A. Cammarato and A. J. Engler, *Biophys. J.*, 2011, **101**, 2629–2637.
3 S. Guo and B. B. Akhremitchev, *Biomacromolecules*, 2006, **7**, 1630–1636.
4 J. Hellwig, V. L. Durán and T. Pettersson, *Anal. Methods*, 2018, **10**, 3820–3823.
5 I. N. Sneddon, *Int. J. Eng. Sci.*, 1965, **3**, 47–57.
6 J. L. Hutter and J. Bechhoefer, *Rev. Sci. Instrum.*, 1993, **64**, 1868–1873.
7 F. Rico, P. Roca-Cusachs, N. Gavara, R. Farré, M. Rotger and D. Navajas, *Phys. Rev. E - Stat. Nonlinear, Soft Matter Phys.*, 2005, **72**, 1–10.
8 E. K. Dimitriadis, F. Horkay, J. Maresca, B. Kachar and R. S. Chadwick, *Biophys. J.*, 2002, **82**, 2798–2810.
9 N. Guz, M. Dokukin, V. Kalaparthi and I. Sokolov, *Biophys. J.*, 2014, **107**, 564–575.